

EXPLAINING TEV COSMIC-RAY ANISOTROPIES WITH NON-DIFFUSIVE COSMIC-RAY PROPAGATION

J. PATRICK HARDING

P-23, Los Alamos National Laboratory, Los Alamos, NM 87545, USA

CHRIS L. FRYER

CCS-2, Los Alamos National Laboratory, Los Alamos, NM 87545, USA

AND

SUSAN MENDEL

ISR-2, Los Alamos National Laboratory, Los Alamos, NM 87545, USA

Draft version October 10, 2018

ABSTRACT

Constraining the behavior of cosmic ray data observed at Earth requires a precise understanding of how the cosmic rays propagate in the interstellar medium. The interstellar medium is not homogeneous; although turbulent magnetic fields dominate over large scales, small coherent regions of magnetic field exist on scales relevant to particle propagation in the nearby Galaxy. Guided propagation through a coherent field is significantly different from random particle diffusion and could be the explanation of spatial anisotropies in the observed cosmic rays. We present a Monte Carlo code to propagate cosmic particle through realistic magnetic field structures. We discuss the details of the model as well as some preliminary studies which indicate that coherent magnetic structures are important effects in local cosmic-ray propagation, increasing the flux of cosmic rays by over two orders of magnitude at anisotropic locations on the sky. The features induced by coherent magnetic structure could be the cause of the observed TeV cosmic-ray anisotropy.

Subject headings: astroparticle physics, magnetic fields, turbulence, ISM: cosmic rays, ISM: kinematics and dynamics

1. INTRODUCTION

At high energies, cosmic ray particles are one of the most important handles for understanding the Galaxy; the energy density of cosmic rays is similar to that of Galactic magnetic fields and starlight. However, the sources of the cosmic rays remain a mystery. Many sources, from active galactic nuclei and supernovae to dark matter annihilation have all been postulated as the origin of the measured cosmic rays. Because cosmic rays are charged, they do not point back to their sources, so in order to understand their creation, one must understand the process of cosmic-ray propagation. Local measurements of cosmic rays have shown several signatures which cannot be explained by standard astrophysical propagation models. In order to understand the significance of these signatures and the sources of these cosmic rays, we propose a new framework for modeling cosmic-ray propagation.

Current propagation codes, such as GALPROP (Strong and Moskalenko (1998)), tend to focus on the diffusive regime of particle propagation, considering particle diffusion and losses in the regime where the magnitude of the magnetic field is relevant but not the direction, i.e. the diffusion limit. For particles which propagate over large regions of space ($\gtrsim 100$ pc), the magnetic field may be dominated by a stochastic, chaotic component which does have this behavior (Giaccinti and Sigl (2012)). However, even in these regions,

the strength of magnetic turbulence is typically smaller than that of the guiding field, so the coherent field may still play an important role (Gaensler et al. (2011)). This can be seen in studies of pitch-angle scattering in large interstellar coherent magnetic structures (Barge et al. (1984); Desiati and Zweibel (2014)) and in studies of parallel and perpendicular diffusion (Giacalone and Jokipii (1999); Tautz et al. (2013, 2014); Hussein et al. (2015); Shalchi (2015)). We plan on incorporating these cross-fieldline transport effects into our framework in the future.

Over propagation distances smaller than those considered in these papers, such as those relevant for cosmic rays observed at energies above the TeV scale, the magnetic fields can also have strong spatial correlations; the magnetic fields which affect the local galaxy can be coherent, as opposed to the chaotic, stochastic magnetic fields believed to dominate throughout the galaxy on larger scales (Frisch and Schwadron (2014); Frisch et al. (2015a,b)). Some indications of these coherent magnetic structures, which can have correlation length of tens of parsecs, have been observed, such as those from the heliotail or the recently-observed features by IBEX (Schwadron et al. (2014)) (though the features in that paper are given in terms of a diffusive model). It is the nondiffusive regime of cosmic-ray propagation that we consider here.

When particles see these small-scale magnetic structures, their propagation is much different than in the standard chaotic fields. Using a combination of discrete diffusion Monte Carlo and direct Monte Carlo, we simulate cosmic-ray propagation including both the mag-

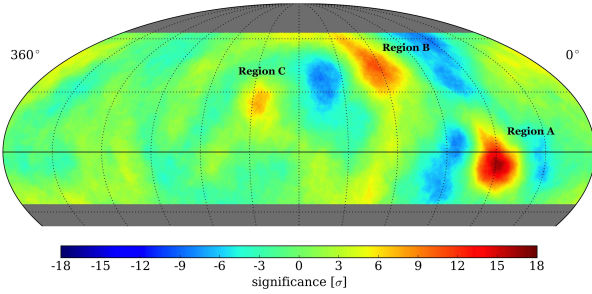


FIG. 1.— The observed anisotropy of hadronic cosmic rays as seen by HAWC (Abeysekara et al. (2014)). Three regions of significant excess over the background (Regions A, B, and C) are observable on scales of less than ten degrees on the sky.

netic field strength and direction. By including the magnetic field direction, we are able to account for coherent features in the magnetic field and correlations between nearby regions in magnetic field strength.

2. PHYSICAL MOTIVATION

One particular observation that has motivated this propagation code is the TeV cosmic-ray anisotropy. Anisotropies in the arrival directions of TeV cosmic rays (CRs) have been observed by many experiments, both on large angular scales (Amenomori et al. (2005); Amenomori (2006); Guillian et al. (2007); Abdo et al. (2009); Aglietta et al. (2009); Zhang et al. (2009); Amenomori et al. (2010); Munakata et al. (2010); Abbasi et al. (2010); de Jong (2012); Cui (2011); Aartsen et al. (2013); Bartoli et al. (2015)) and small angular scales (Amenomori et al. (2007); Abdo et al. (2008); Abbasi et al. (2011); Aartsen et al. (2013); Di Sciascio (2013); Bartoli et al. (2013); Abeysekara et al. (2014)). The observed small-scale cosmic-ray anisotropy from the High Altitude Water Cherenkov (HAWC) collaboration (Abeysekara et al. (2014)) is shown in figure 1. While a large-scale dipole anisotropy is expected from asymmetries in source distributions, the source of the small-scale anisotropic CRs remains a mystery. It appears that the small-scale anisotropy may be made up mostly of hadrons (Abdo et al. (2008)), but the gyroradius of a TeV proton in the local magnetic field is only a few milliparsecs, which is much closer than any currently-known candidate source of CRs. Even the neutron decay length of 0.1 parsecs is thousands of times smaller than the nearest known supernova remnant, the Geminga pulsar. The energy spectrum of the anisotropic CRs is also significantly harder than the spectrum of isotropic CRs.

Production of a localized hadronic region of CRs requires anisotropic CR propagation, as CRs from any source further than 0.1 parsec from the Earth are made nearly isotropic through diffusive propagation to the Earth. Several sources of the CR anisotropy have been considered, including magnetic mirrors (Drury and Aharonian (2008)), anisotropic turbulence (Malkov et al. (2010)), a local source in the heliotail (Lazarian and Desiati (2010)), strangelets (Kotera et al. (2013)), turbulent mixing from the large scale anisotropy (Giacinti and Sigl (2012)), and nearby dark matter subhalos (Harding

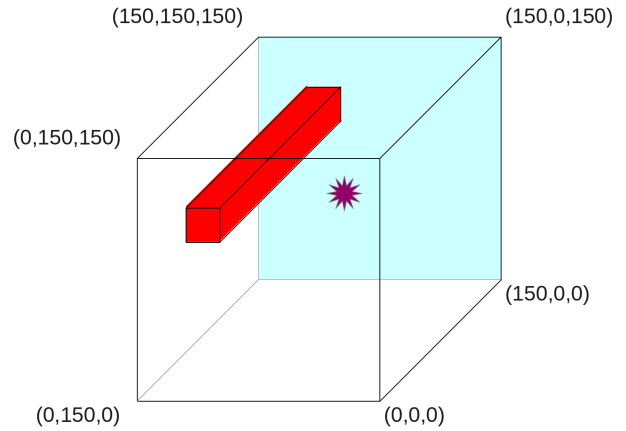


FIG. 2.— A schematic of the source, located at $(x, y, z) = (75 \text{ pc}, 75 \text{ pc}, 75 \text{ pc})$ (magenta star) and the coherent magnetic field $a_{\min} < y, z < a_{\max}$ (red tube). The $x = 150 \text{ pc}$ wall (in blue) is our proxy for the Earth sky. Note that in our figures of the $x = 150 \text{ pc}$ wall, the coordinates of the y -axis go from left-to-right instead of right-to-left.

(2013)). Most of these explanations, however, require anisotropic cosmic-ray propagation. Many of these explanations of the cosmic-ray anisotropy require limited particle diffusion, such as that through a local coherent magnetic field structure. By including this magnetic field structure in the cosmic ray propagation, we propose to test several of the source populations and magnetic field configurations that can explain the TeV cosmic-ray anisotropy and quantify which features can reproduce the observed anisotropy.

Another relevant measurement which cannot be explained with standard astrophysical cosmic rays is the observation of an excess in local cosmic-ray positrons (Adriani et al. (2011); Ackermann et al. (2012); Aguilar et al. (2013)). The origin of these positrons is currently unknown, with explanations ranging from nearby pulsars (Linden and Profumo (2013)) to exotic explanations like dark matter annihilation (Cholis and Hooper (2013)). However, the questions remain of how far the source of these positrons is from the Earth and the spectrum of their source, both of which are intimately tied to the propagation of the positrons in the local neighborhood.

3. THE GEOMETRY OF THE CODE

This code is designed for propagation of highly relativistic particles, which move near to the speed of light. Specifically, the code is designed to work only for particles with $v \approx c$ and will finish propagation in the case that the particles energy drops low enough to make the particle speed appreciably lower than c . These particles travel long distances before losing an appreciable amount of energy. The code is currently set up to work with cosmic-ray electrons, positrons, protons, and ions, but here we only consider cosmic-ray protons, which are expected to be the dominant form of cosmic rays with TeV-PeV energies creating the observed cosmic-ray anisotropies.

The code is based on a 3-dimensional grid of cells, with the physical properties constant within each cell. The cells are set to be much larger than the scattering length

of each cosmic ray and much larger than the Larmor radius of the particle. Each cell has several properties which are allowed to vary cell-to-cell, including the particle density, particle temperature, hydrogen and helium fraction, turbulent magnetic field strength, scale of the turbulent magnetic field coherence length, and coherent magnetic field strength and direction. Each simulated cosmic ray is then propagated through these cells. Characteristic values for these parameters are shown in table 1. For the calculations in this paper, we consider cubic cells with 3 pc spacing, though any spacing which is much larger than the particle’s mean-free-path (for chaotic fields) and larger than the particle Larmor radius (for coherent fields) could be used. The walls of the simulation act as absorption boundaries, with particle propagation ending once the particle hits one of these bounding walls.

For our first simple geometry, we consider two regions, one outside of the coherent field and one within the coherent field. Our coherent field region passes along the x-direction between $a_{\min} < y, z < a_{\max}$. For a schematic, see figure 2. For the simple case shown here, we assume that there is no coherent field outside of this region, only turbulent fields. We also assume there is no turbulent field within this region, only coherent fields. This neglects the effects of scattering within regions with coherent fields, such as particle feedback within the coherent region producing a small turbulent magnetic field. It is therefore not a definitive study of the geometries which will produce the observed anisotropy, but rather a test geometry for the code which indicates that such coherent fields could be important for studies of cosmic ray anisotropies. How the inclusion of turbulent components with coherent components will affect the results will be studied in a follow-up paper. However, the authors believe that the qualitative behavior will not change and that the quantitative behavior should be similar. This is because many of the particles which may scatter out of the coherent-dominated region will scatter back into it. Also, the difference in timescales between turbulent and coherent motion (linear versus square root in time) means that particles will travel a long way along coherent streams before scattering out of the coherent-dominated region.

The source distribution allows for multiple sources with varying spectra and particle-type production. For simplicity, however, herein we consider a single source located at $(x, y, z) = (75 \text{ pc}, 75 \text{ pc}, 75 \text{ pc})$ in the center of our simulation region. Our simple particle spectrum is 100% protons all of which start with 10 TeV of energy.

4. PARTICLE PROPAGATION

The propagation of particles through the intergalactic medium involves a variety of particle processes, including particle-particle collisions and interaction of charged particles with magnetic fields, which affect the trajectory of the particle’s path and energy losses. Here we discuss an overview of how the code deals with particle propagation, with further details in later sections.

At the beginning of the transport, the particle energy, starting location, type, and direction are determined randomly from the input sources. The particle is looped over coarse timesteps. For each coarse timestep, the cell position of the particle is found, along with the param-

n	n_e	$k_B T$	x_H	x_{He}	λ_{\max}	b_t	$ \vec{B}_{\text{coh}} $
0.01 cm^{-3}	0.01 cm^{-3}	10^{-4} MeV	0.9	0.1	10^{15} cm	$0 \mu\text{G}$, $3 \mu\text{G}$	$0 \mu\text{G}$, $3 \mu\text{G}$

TABLE 1
TABLE OF THE CHARACTERISTIC VALUES FOR THE PARAMETERS IN THE CELLS. THE PARAMETERS ARE, IN ORDER: THE COMBINED NUMBER DENSITY OF NEUTRAL HYDROGEN AND HELIUM, THE NUMBER DENSITY OF IONIZED ELECTRONS, THE PARTICLE TEMPERATURE, THE HYDROGEN FRACTION, THE HELIUM FRACTION, THE TURBULENT MAGNETIC FIELD SCALE LENGTH, THE MAXIMUM TURBULENT FIELD STRENGTH, AND THE COHERENT FIELD STRENGTH. THESE PARAMETERS ARE ROUGHLY EQUIVALENT TO THE VALUES IN THE LOCAL BUBBLE (FRISCH (1995)). FOR CELLS OUTSIDE OF OUR COHERENT FIELD, THE COHERENT FIELD STRENGTH IS $0.0 \mu\text{G}$ AND THE TURBULENT FIELD STRENGTH IS $3 \mu\text{G}$ (KISTLER ET AL. (2012)). INSIDE OUR SIMPLE COHERENT FIELD, THE TURBULENT FIELD STRENGTH IS $0.0 \mu\text{G}$ AND THE COHERENT FIELD STRENGTH IS $3 \mu\text{G}$ ALONG THE X-DIRECTION.

eters for that cell. If there is a coherent magnetic field in the cell, then the transport Monte Carlo propagates the particle until either the coarse timestep is over or the particle leaves the cell. If there is no coherent magnetic field in the cell, then the discrete diffusion Monte Carlo is used to propagate the particle until either the coarse timestep is over or the particle leaves the cell. After each timestep, the energy losses for the particle over this time are calculated. This process is repeated over timesteps and cells until the particle exits the simulation.

It is important to note that while the studies in this paper consider coherent and diffusive magnetic fields separately, in all regions in space both of these effects contribute to the particle motion. Additionally, there is not a distinction between “single-particle” motion and “ensemble diffusive” motion in the trajectories of true particles. Even for regions of space in which the ensemble behaves diffusively, individual particles actually have deterministic trajectories. Particularly over distances of less than a single scattering length, these deterministic propagation effects can be seen. This is part of the purpose of this propagation code - to show the effects which are often neglected in diffusion-only codes.

4.1. Particle Transport Monte Carlo

The particle transport Monte Carlo follows each particle as it traverses each cell and passes into the adjacent cell. Within each cell, chaotic fields are assumed to be coherent over their small coherence length, so over these short distances the particle motion can be solved exactly. Particles within a magnetic field of strength B , energy E , and charge Ze have a Larmor radius

$$r_L = 1.1 \times 10^{-9} \text{ pc}^{-1} Z^{-1} (E/\text{MeV}) (B/\mu\text{G})^{-1}. \quad (1)$$

The equation of motion for this particle is (Kistler et al. (2012))

$$\frac{d\vec{v}}{dt} = \frac{c}{r_L} \vec{v} \times \hat{B}, \quad (2)$$

where \hat{B} is the direction of the net magnetic field (coherent and turbulent) and $|\vec{v}| = c$. For our calculations, we choose time in years and distance in parsecs ($c \approx 0.31 \text{ pc/yr}$).

The equation of motion can be solved analytically, over the time in which the particle traverses a single coherent region of the turbulent magnetic field. This is most easily

done in a coordinate system with an axis along the magnetic field. For our calculations, we use the coordinates $(\hat{i}, \hat{j}, \hat{k})$ with

$$\hat{j} = \hat{B} = \left(\frac{B_x}{B} \quad \frac{B_y}{B} \quad \frac{B_z}{B} \right) \quad (3)$$

$$\begin{aligned} \hat{k} &= \frac{\hat{v}_0 \times \hat{B}}{|\hat{v}_0 \times \hat{B}|} \\ &= \left(\frac{v_{0y}B_z - v_{0z}B_y}{|v_0 \times B|} \quad \frac{v_{0z}B_x - v_{0x}B_z}{|v_0 \times B|} \quad \frac{v_{0x}B_y - v_{0y}B_x}{|v_0 \times B|} \right) \end{aligned} \quad (4)$$

$$\begin{aligned} \hat{i} &= \hat{j} \times \hat{k} = \hat{B} \times \frac{\hat{v}_0 \times \hat{B}}{|\hat{v}_0 \times \hat{B}|} \\ &= \left(\frac{B^2 v_{0x} - B_x(v_0 \cdot \vec{B})}{B|v_0 \times B|} \quad \frac{B^2 v_{0y} - B_y(v_0 \cdot \vec{B})}{B|v_0 \times B|} \quad \frac{B^2 v_{0z} - B_z(v_0 \cdot \vec{B})}{B|v_0 \times B|} \right), \end{aligned} \quad (5)$$

with \hat{v}_0 the initial direction of the particle velocity. We refer to the j-component of the initial velocity (along the direction of \vec{B}) as v_{\parallel} and the magnitude of the initial velocity perpendicular to the magnetic field as v_{\perp} ($v_{\perp} = \sqrt{v_0^2 - v_{\parallel}^2}$). Note that at $t = 0$, the initial velocity is entirely along the \hat{i} and \hat{j} directions. After a time t , the velocity is

$$v_i = v_{\perp} \cos(ct/r_L) \quad (6)$$

$$v_j = v_{\parallel} \quad (7)$$

$$v_k = v_{\perp} \sin(ct/r_L) . \quad (8)$$

To get the results in the original (x, y, z) -coordinates, we need to project these values back into the (x, y, z) -space, using the components given in equations 3-5.

A similar calculation to the particle velocity can be done to calculate the particle position as well. However, for problems in which the Larmor radius is much smaller than the cell size and the mean-free-path, the motion orthogonal to the magnetic field can be neglected and the equation simplifies. In this case, which applies to the geometry we consider herein, the particle follows the magnetic field with a velocity

$$\vec{x}(t) = \vec{x}_0 + v_{\parallel} t \hat{B} = \vec{x}_0 + \frac{\vec{v}_0 \cdot \vec{B}}{B} t \hat{B} . \quad (9)$$

In this case, however, the full path length traversed by the particle, which is needed to account for absorption, is given by ct . Note that we consider the particle's energy to remain constant within each cell, which is a reasonable approximation for the short distances and high energies we consider here. We also have assumed ultra-relativistic particles, with $v \approx c$ during the propagation. For low-energy particles or extremely large cells, these approximations may no longer be valid.

The particle transport in regions of a coherent magnetic field is driven by taking steps over which the turbulent magnetic field is constant (Petrosian and Liu (2004)). Even though turbulent magnetic fields have small coherence lengths, over these lengths they can be thought of as coherent. We determine the distance that a particle travels before it encounters a change in the

turbulent magnetic field following Fryer et al. (2007):

$$\begin{aligned} k_{sc} &= 1/\lambda_{sc} \\ &= 4.7 \times 10^{12} \text{ pc}^{-1} \left(\frac{\lambda_{\max}}{\text{cm}} \right)^{-1/2} \left(\frac{B_t}{\mu\text{G}} \right)^{1/2} \left(\frac{E_{\text{prot}}}{\text{MeV}} \right)^{-1/2} \end{aligned} \quad (10)$$

where λ_{\max} is the scale length of the turbulent field, B_t is the amplitude of the turbulent magnetic field, and E_{prot} is the proton energy. Note that B_t , the instantaneous amplitude of the turbulent magnetic field, should not be confused with the maximum amplitude of the turbulent magnetic field b_t .

We also consider the possibility of the particle being absorbed into the ISM, which provides an additional opacity. This is due to scattering on nuclei and is proportional to the total number density of nuclei (not nucleons) to scatter with. We parameterize this absorption using (Fryer et al. (2007))

$$k_{\text{abs}} = 1/\lambda_{\text{abs}} = 9.9 \times 10^{-8} \text{ pc}^{-1} (n/\text{cm}^{-3}) . \quad (11)$$

This accounts for all particle absorption on the ISM. This absorption is determined solely by the number density of ISM particles within each cell and therefore does not change until the particle leaves the cell. In the ISM $k_{sc} \gg k_{\text{abs}}$, though in general this could change for high-density, low-magnetic field regions.

The time that a particle can travel before either the turbulent component of the magnetic field changes or the particle gets absorbed is

$$t_{\text{step}} = -\ln \left(\frac{\chi}{c(k_{sc} + k_{\text{abs}})} \right) , \quad (12)$$

where χ is a standard deviate sampled between 0 and 1. This comes from the exponential nature of both the absorption and magnetic field coherence length with distance travelled by the particle.

When a particle's trajectory would take it out of its current cell and into the next cell, the code instead scales back the particle's position so as to just barely enter the next cell. In doing this, there is an implicit assumption on the particle steps being drawn from the same distribution, even though in practice some of those steps are shorter than probability would suggest. However, this should not strongly affect the results of the simulation, especially in the limit that the particle takes many steps before exiting each cell.

Within this region of coherent magnetic field, the particle propagates in a way which is dramatically different from diffusion. The particle is strongly biased to move in a single direction, along the coherent magnetic field, and travels in that direction quickly, with a mean-free-path which is proportional to the time-of-flight, as opposed to the square root of the time-of-flight which diffusion does.

4.2. Discrete Diffusion Monte Carlo

In regions where there is no coherent magnetic field, the chaotic magnetic fields change direction on a scale much smaller than the grid spacing of the code. The particles require many small, random-walk steps to reach the edge of a cell-wall. In these regions, a diffusion approximation is valid. To calculate the behavior of a cosmic ray in the diffusive regime, we use discrete diffusion Monte

Carlo (DDMC) methods. In DDMC, many of the smaller random-walk steps which would be taken by the particle are combined together into larger groups of steps. These steps are drawn at random from a distribution of particle locations after N steps. Specifically, we choose N such that it will take several of these DDMC steps to leave a given cell. However, this speeds up the code over direct Monte Carlo calculation by many orders of magnitude. Effectively, the code recalculates the diffusion coefficient in each cell, according to the equations derived below. This allows the geometry to, in principle, have a different turbulent field amplitude in each cell, though in this study each cell outside of the coherent field region the same turbulent field amplitude. Inside the coherent field region, for this study, we assume the turbulent field amplitude is zero.

The particle diffusion is done according to a standard three-dimensional random walk according to the diffusion coefficient within each cell. To calculate the diffusion coefficient in each cell, we ran our particle transport Monte Carlo for many particles, on the assumption that even turbulent magnetic fields are coherent on distances much shorter than their coherence length. We then averaged over those particles' motion according to the equations described below, in order to calculate the appropriate diffusion behavior in each cell according to the strength of its turbulent field.

While the properties of coherent magnetic field \vec{B}_{coh} have their amplitude and direction fixed by the input geometry, the turbulent magnetic field \vec{B}_{turb} varies step-by-step throughout the propagation. For the turbulent magnetic field, we assume that each \vec{B}_{turb} value is sampled at random. (This is the real-space analog of a Kolmogorov spectrum). Note that this is different from sampling a random *amplitude* of the turbulent magnetic field from a flat distribution. For a random vector in three dimensions ($B_{\text{turb}}, \theta, \phi$) the amplitude B_{turb} , polar angle θ , and azimuthal angle ϕ are sampled as

$$B_{\text{turb}} = b_t \chi_1^{1/3} \quad (13)$$

$$\cos(\theta) = 2\chi_2 - 1 \quad (14)$$

$$\phi = 2\pi\chi_3 \quad (15)$$

with χ_i standard deviates between 0 and 1. The maximum allowed value of the turbulent field amplitude b_t sets the scale for allowed values of the magnetic field. This gives a mean amplitude of the turbulent magnetic field of $\langle B_{\text{turb}} \rangle = 0.75b_t$.

For a three-dimensional random walk with typical distance per step a , the probability of moving distance r after N steps is the three-dimensional Gaussian

$$P(r; N) = 4\pi r^2 \left(\frac{3}{2\pi N a^2} \right)^{3/2} \exp\left(-\frac{3r^2}{2N a^2} \right) \quad (16)$$

This can be most easily calculated by sampling three one-dimensional Gaussian random variables g_1, g_2, g_3 centered at 0 with widths $\sqrt{N a^2/3}$ and adding them in quadrature:

$$g_{3D} = \sqrt{g_1^2 + g_2^2 + g_3^2} \quad (17)$$

where Gaussian random variables are calculated using, e.g., a Box-Muller transform. The direction is then given

using a polar and azimuthal angle sampled as in equations 14 and 15.

The typical distance for each step follows a similar equation for each step of the transport routine (equation 12), but averaged over many steps. Because the magnetic field changes in each step, thereby changing the value of K_{sc} , this must be taken into account as well. The correct value of a is the expectation value for displacement in a single step, given by

$$a = \sqrt{\langle \vec{r}^2 \rangle} - \langle \vec{r} \rangle^2 = \sqrt{\langle \vec{r}^2 \rangle} \quad (18)$$

For simplicity, we assume that the energy change of the particle over a step is negligible. For convenience, we also define a dimensionless parameter

$$\xi \equiv \frac{k_{\text{sc}}(B_t = b_t)}{k_{\text{abs}}} \quad (19)$$

where k_{sc} (equation 10) is evaluated at the maximum turbulent magnetic field b_t and k_{abs} is calculated as in equation 11. For the magnetic field of equation 13, the expectation value of the step size is

$$a = \frac{\sqrt{2}}{k_{\text{abs}}} \left[\frac{3}{2}\xi^{-2} - 4\xi^{-3} + 9\xi^{-4} - 24\xi^{-5} + 6\frac{\xi^{-6}}{1+\xi} + 30\xi^{-6} \ln(1+\xi) - 6\xi^{-6} \right]^{1/2} \quad (20)$$

In the limiting cases of large ξ ($k_{\text{sc}} \gg k_{\text{abs}}$) and small ξ ($k_{\text{abs}} \gg k_{\text{sc}}$), this simplifies to

$$a \approx \frac{\sqrt{3}}{k_{\text{sc}}(B_t = b_t)}, \quad \xi \rightarrow \infty \quad (21)$$

$$a \approx \frac{\sqrt{2}}{k_{\text{abs}}}, \quad \xi \rightarrow 0 \quad (22)$$

The value of a , in equation 16, determines the typical displacement of the particle after N steps.

To determine whether the particle was absorbed into the ISM after these N steps, we must determine the amount of time that the propagation took, or equivalently, the path-length of the particle's motion. Rather than the values $\langle \vec{r}^2 \rangle$ and $\langle \vec{r} \rangle$ which went into equation 18, the path length is evaluated as $\langle |\vec{r}| \rangle$. Following a similar calculation to equation 20, we find that the typical path length for each step is

$$\langle |\vec{r}| \rangle = \frac{1}{k_{\text{abs}}} \left[\frac{6}{5}\xi^{-1} - \frac{3}{2}\xi^{-2} + 2\xi^{-3} - 3\xi^{-4} + 6\xi^{-5} - 6\xi^{-6} \ln(1+\xi) \right] \quad (23)$$

In the limiting cases of large ξ ($k_{\text{sc}} \gg k_{\text{abs}}$) and small ξ ($k_{\text{abs}} \gg k_{\text{sc}}$), this simplifies to

$$\langle |\vec{r}| \rangle \approx \frac{6}{5k_{\text{sc}}(B_t = b_t)}, \quad \xi \rightarrow \infty \quad (24)$$

$$\langle |\vec{r}| \rangle \approx \frac{1}{k_{\text{abs}}}, \quad \xi \rightarrow 0 \quad (25)$$

The probability that the particle was absorbed by the ISM is

$$P_{\text{abs}}(N) = \exp(-k_{\text{abs}}N\langle |\vec{r}| \rangle) \quad (26)$$

and the time taken for the N steps is

$$\Delta t_N = N\langle |\vec{r}| \rangle/c \quad (27)$$

When a particle's trajectory would take it out of its cell and into another, the trajectory is scaled back, similar to what is done during the particle transport routine discussed in section 4.1. However, because the displacement is proportional to the square root of the number of steps, the number of steps is scaled back quadratically to get the propagation distance and time. To propagate over the distance from the source to the boundary wall (75 – 130 pc) takes a typical particle 4-20 million years.

4.3. Ion Energy Losses

After each time step in the transport and diffusion processes, we calculate the energy losses for the particle. For relativistic nucleons in a charged plasma, such as the ISM, the energy losses are dominated by Coulomb scattering and ionization of the medium. We calculate the energy losses for ions in our simulation as a continuous process, following Strong and Moskalenko (1998). Energy losses from Coulomb collisions are given by (Mannheim and Schlickeiser (1994))

$$\left(\frac{dE}{dt}\right)_{\text{Coulomb}} \approx -4\pi r_e^2 c m_e c^2 Z^2 n_e \ln \Lambda \frac{\beta^2}{x_m^3 + \beta^3}, \quad (28)$$

where $r_e = 2.8 \times 10^{-13}$ cm is the classical electron radius, $m_e c^2 = 0.511$ MeV is the electron mass, Ze is the charge of the incoming ion, $\beta = v/c$ is the speed of the incoming ion, and n_e is the number density of electrons in the plasma. The temperature of the electrons in the plasma, T_e , comes in as

$$x_m \equiv \left(\frac{3\sqrt{\pi}}{4}\right)^{1/3} \sqrt{\frac{2k_B T_e}{m_e c^2}}, \quad (29)$$

with k_B the Boltzmann constant. The Coulomb logarithm $\ln \Lambda$ accounts for all possible scattering angles of the incident ion with the electron (Dermer (1985)). Because the incoming ion and the plasma electron are non-identical particles, the maximum scattering angle is π (for identical particles, it would be $\pi/2$). The minimum scattering angle is given by the excitation of a plasmon with the plasma frequency. For a cold plasma in the Born regime, which is appropriate for the ISM, this is given in equation B7 of Dermer (1985). The corresponding Coulomb logarithm is

$$\ln \Lambda \approx \frac{1}{2} \ln \left(\frac{m_e^2 c^4}{\pi r_e \hbar^2 c^2 n_e} \frac{M \gamma^2 \beta^4}{M + 2\gamma m_e} \right), \quad (30)$$

where \hbar is the reduced Planck constant, M is the incoming ion mass, and γ is the incoming ion Lorentz factor. Note that in calculating the energy losses, we account for the true speed of the incoming ion, using

$$\gamma = \frac{E}{M c^2} \quad (31)$$

$$\beta = \sqrt{1 - \frac{1}{\gamma^2}}. \quad (32)$$

The other primary source of energy loss for relativistic ions is through ionization of the neutral plasma. This follows the Bethe-Bloch formula (Strong and Moskalenko

model designation	A	B	C	D
a_{\min} (pc)	111	111	81	138
a_{\max} (pc)	120	114	84	141
distance from source (pc)	57.3	53.0	10.6	91.2

TABLE 2

DESCRIPTION OF THE MODELS OF COHERENT MAGNETIC FIELD. THE COHERENT FIELD IS A REGION WHICH IS $a_{\min} < y, z < a_{\max}$ AND POINTS IN THE X-DIRECTION (TOWARD EARTH). THE DISTANCE FROM THE SOURCE TO CENTER OF EACH COHERENT MAGNETIC FIELD IS SHOWN AS WELL.

model designation	A	B	C	D
particle density at Earth (prot/sr)	1.6 $\times 10^7$	1.0 $\times 10^8$	2.8 $\times 10^8$	2.9 $\times 10^7$
particle density, no coherent field (prot/sr)	1.5 $\times 10^5$	1.8 $\times 10^5$	2.6 $\times 10^5$	1.9 $\times 10^4$
increased brightness over no coherent field	110 \times	560 \times	1080 \times	1500 \times

TABLE 3

THE DETAILS OF THE PARTICLE DENSITY OBSERVED IN THE SKY TOWARD THE MAGNETIC FIELD REGION FOR EACH CONSIDERED GEOMETRY. THE SIMULATION RESULTS WERE CALCULATED FROM 2×10^6 SAMPLED 10 TeV PROTONS. THE MODELS OF COHERENT MAGNETIC FIELD IN THE FIRST ROW ARE GIVEN IN TABLE 2. THE SECOND ROW GIVES THE PARTICLE DENSITY (PARTICLES/SR) WHICH ARRIVES AT THE $x = 150$ pc WALL, WHICH IS OUR PROXY FOR THE EARTH SKY. THE THIRD ROW GIVES THE PARTICLE DENSITY AT THAT SAME LOCATION IN A SIMULATION WITH NO COHERENT MAGNETIC FIELD, FOR COMPARISON. THE RATIO OF THE PARTICLE DENSITY WITH AND WITHOUT THE COHERENT FIELD IS GIVEN IN ROW FOUR. (SEE SECTION 5.1 FOR MORE DETAILS.)

(1998); Mannheim and Schlickeiser (1994)):

$$Q_{\max} = \frac{2m_e c^2 \beta^2 \gamma^2}{1 + 2\gamma \frac{m_e}{M} + \frac{m_e^2}{M^2}} \quad (33)$$

$$B_H = \ln \left[\frac{2m_e c^2 \beta^2 \gamma^2 Q_{\max}}{(19 \text{ eV})^2} \right] - 2\beta^2 \quad (34)$$

$$B_{\text{He}} = \ln \left[\frac{2m_e c^2 \beta^2 \gamma^2 Q_{\max}}{(44 \text{ eV})^2} \right] - 2\beta^2 \quad (35)$$

$$\left(\frac{dE}{dt}\right)_{\text{Ionization}} = -2\pi r_e^2 c m_e c^2 Z^2 \frac{1}{\beta} n \times (x_H B_H + 2x_{\text{He}} B_{\text{He}}), \quad (36)$$

where Q_{\max} is the kinematic maximum energy transfer to the atomic electron, 19 eV is the ionization energy of neutral hydrogen, 44 eV is the ionization energy of neutral helium, n is the combined number density of neutral hydrogen and helium, x_H and x_{He} are the fraction of the neutral gas made up of hydrogen and helium, and we have accounted for the two ionizable electrons on the helium atoms. Because $M \gg m_e$, we neglect the quadratic term in Q_{\max} in our calculations. Other energy losses are negligible for highly relativistic ions. For proton ions travelling through the ISM, ion fragmentation and decay are not considered.

5. RESULTS

To test how a region of coherent magnetic field would affect propagating cosmic rays, we have run several simulations with varying locations and spatial sizes of coherent magnetic fields. All the tests were run within a

model designation	A	B	C	D
fraction particles within coherent field	12%	9.0%	46%	1.2%
geometric $\Omega/4\pi$ of coherent field	2.8%	0.93%	5.7%	0.41%
increased particles trapped from scattering	$4.3\times$	$9.7\times$	$8.1\times$	$2.9\times$

TABLE 4

THE RELATIVE IMPORTANCE OF PARTICLES WHICH SCATTER INTO THE MAGNETIC FIELD COMPARED TO JUST THE GEOMETRIC SOLID ANGLE IT SUBTENDS FROM THE SOURCE. THE SIMULATION RESULTS WERE CALCULATED FROM 2×10^6 SAMPLED 10 TEV PROTONS. THE MODELS OF COHERENT MAGNETIC FIELD IN THE FIRST ROW ARE GIVEN IN TABLE 2. ROW TWO GIVES THE FRACTION OF THE ISOTROPIC FLUX WHICH IS ABSORBED INTO THE COHERENT MAGNETIC FIELD. ROW THREE GIVES THE FRACTION OF THE TOTAL 4π SOLID ANGLE WHICH IS SUBTENDED BY THE COHERENT MAGNETIC FIELD. ROW FOUR GIVES THE RATIO OF THE TOTAL ACCEPTANCE OF PARTICLES INTO THE COHERENT REGION TO THE GEOMETRIC SOLID ANGLE. THIS IS INDICATIVE OF THE IMPORTANCE OF PARTICLES WHICH SCATTER INTO THE COHERENT FIELD. (SEE SECTION 5.3 FOR MORE DETAILS.)

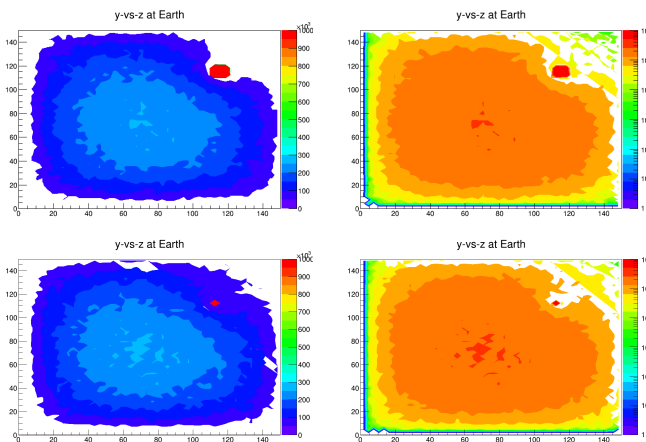


FIG. 3.— A comparison of models A (top) and B (bottom) of table 2. This compares the effect of physical extent of the region of coherent magnetic field on particle propagation. The axes are y and z at the $x = 150$ pc wall, which is our proxy for the Earth sky, and the color scale is in particles/sr, shown both linearly (left) and logarithmically (right). The plots were made with 2×10^6 sampled 10 TeV protons. The bright red spot in the upper right quadrant of the figures is the location of the coherent magnetic field. Of particular note is the region with a deficit of particles surrounding the coherent magnetic field and to its upper right. This is caused by the high probability of particles which would enter these regions first scattering into the coherent magnetic field. For more on this, see section 5.4.

$150 \text{ pc} \times 150 \text{ pc} \times 150 \text{ pc}$ box, with a grid spacing of 3 pc. For all of the tests, we assume a source located at the center of the box (at $(75 \text{ pc}, 75 \text{ pc}, 75 \text{ pc})$) emitting monochromatic particles with an energy of 10 TeV. The simulated cosmic rays are 100% protons. All physical parameters of the ISM are given in table 1. We assume a region of coherent magnetic field which is uniform in the x -direction and contained to a finite region $a_{\min} < y, z < a_{\max}$ in the y - and z -directions. The specific magnetic field regions considered are listed in table 2. For the parameters modeled, the energy losses of the protons were small

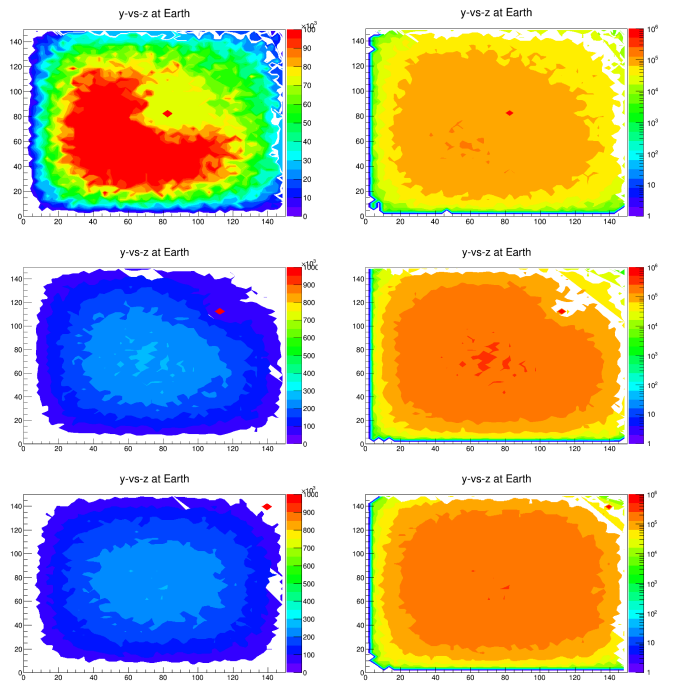


FIG. 4.— A comparison of models C (top), B (middle), and D (bottom) of table 2. This compares the effect of distance from the source to the region of coherent magnetic field on particle propagation. The axes are y and z at the $x = 150$ pc wall, which is our proxy for the Earth sky, and the color scale is in particles/sr, shown both linearly (left) and logarithmically (right). Note that the linear-scale plot for model C only goes up to 10^5 , unlike the rest of the figure which have color scales up to 10^6 . (This was done to highlight the deficit region in this figure. On a scale up to 10^6 , this figure has a bright red spot on a monochrome blue background.) The plots were made with 2×10^6 sampled 10 TeV protons. The bright red spot in the upper right quadrant of the figures is the location of the coherent magnetic field. Similar to figure 3, there is a region with a deficit of particles surrounding the coherent magnetic field and to its upper right. This effect becomes much stronger as the coherent magnetic field is moved closer to the source. For more on this, see section 5.5.

($\sim 1 - 10$ MeV) and did not appreciably affect the particles' energies.

Our proxy for the anisotropies seen in the sky at Earth is the $x = 150$ pc wall of our simulation. This models the case where a region of coherent magnetic field stretches from the general vicinity of a cosmic-ray source to dump its particles near to the Earth. We consider the relative particle density per solid angle, which corresponds to the signals observed over given solid angle in the sky from Earth.

This study is designed to show the plausibility of such coherent magnetic fields to reproduce anisotropic cosmic-ray features, rather than a full study of how the magnetic field properties affect such features. Therefore, we do not include magnetic field feedback from the cosmic rays or turbulent magnetic fields within the coherent magnetic field region. These effects will be included in a follow-up publication (Harding and Fryer (2015)).

5.1. Increased Particle Density within the Coherent Field

While the particles' diffusion causes a smooth, dipole-like distribution on the sky, the particles that get trapped within the region of coherent magnetic field give a much sharper feature on the sky. In this region, the transport of the cosmic rays follows $\vec{v} \times \vec{B}$ and the particles move along the magnetic field quickly, moving linearly with time. Because of this, the particles which enter the region of coherent field tend to not leave the region during their propagation, until they reach the boundary of the simulation. We expect that this is still true if there are turbulent fields within this region, since turbulent diffusion is a slower process, proportional to the square root of propagation time.

With the greater number of particles being deposited within a small solid angle, the flux from such a region is much larger than from a purely diffusive simulation. Compared to the flux expected from pure diffusion, the flux from the coherent magnetic field is increased by 2-3 orders of magnitude. Specific numbers for our four magnetic field models can be found in table 3.

5.2. Generality of the Coherent Magnetic Field Location

One notable feature of the coherent magnetic fields is that the magnetic field does not have to be directly lined up with a source to still give a large flux on the sky. Previously, the idea of coherent magnetic fields causing anisotropies in the sky were considered (Drury and Aharonian (2008)), but it was assumed that these magnetic fields needed to act as a bridge to channel particles between a source and the Earth. However, it seems that these coherent fields act more as a superhighway, moving the particles from one place to another but not necessarily directly aligned with the source itself. The effect is to move the cosmic rays to a location much closer to the Earth, creating in effect a new, closer cosmic-ray source which may have large angular extent and is not necessarily coincident with photon or neutrino signatures of a true astrophysical source. These behaviors can be seen in figures 3 and 4.

5.3. Scattering Increases the Importance of the Coherent Field

Another feature of the coherent magnetic fields is that they actually contain more cosmic rays than one might expect. Because the coherent magnetic field covers a region of the sky through which the source's particles must pass, the expected number of particles within the coherent field could be expected to be proportional to the solid angle from the source subtended by the coherent field. However, when we simulate the cosmic-ray propagation, we find that far more particles are contained within the coherent field than can be explained with geometric solid angle alone. These numbers for our considered geometries are given in table 4.

In addition to the particles which would be caught in the coherent field while traveling radially outward, particles scattering in the turbulent magnetic field will also often scatter into the coherent magnetic field region during their random walk. Once inside the coherent field, these particles are transported quickly along the field and cease their random walk. Therefore, these scattered par-

ticles increase the number trapped by the coherent field over just a geometric value. Depending on the model, this increase can be 3-10 times the geometric area, and is typically a more important effect for smaller coherent field regions. In figures 3 and 4, the lack of particles which scatter past the coherent magnetic field without passing through it can be seen as a deficit in the distribution in the sky to the upper right of the coherent magnetic field and in its general vicinity.

And intriguing feature of this effect is that as the turbulent fields become stronger, the importance of coherent fields becomes stronger as well, even if the magnetic field strength of the coherent field does not change. So in regions where coherent fields are a *lesser* part of the energy budget, the coherent fields are *more* important for particle propagation behavior.

5.4. The Spatial Size of the Field

Figure 3 shows the sky from two of our coherent magnetic field models - model A and B of table 2. These two models are at similar distances from the source, with the primary difference being their width - model A is 9×9 pc while model B is 3×3 pc. As is shown in table 4, the coherent magnetic field region of model A contains more particles than the small region of model B. However, model B only contains 25% fewer particles than model A, despite model B having a cross-sectional area which is nine times larger. Therefore, the density of particles per solid angle on the sky actually *increases* by nearly an order of magnitude for *smaller* regions of coherent magnetic field.

5.5. The Distance from the Source to the Field

The final effect we studied was how the distance from the source to the coherent magnetic field affected the number of particles trapped within the coherent field. These results, for models B, C, and D, are shown in figure 4. As expected, the number of particles trapped by the coherent magnetic field is largest for models closer to the source, with model C at a distance of 10 pc containing nearly 50% of the total particles output by the source. However, the expected particle density from models with no coherent magnetic field also decreases slightly as you look at sky positions far from the source, and the solid angle for locations near the edge of the wall is slightly smaller than that near the center of the wall. Therefore, although the number of particles within the coherent field decreases by nearly forty times between model C and D (table 4), the particle density in the sky only changes by an order of magnitude. Also, the relative improvement from the coherent magnetic field over no coherent field actually rises (table 3) when the coherent field is very far from the source. For a coherent magnetic field this far from the source to have such a large improvement in particle flux over expected, it is possible that such features are important for diffuse, isotropic cosmic rays as well.

6. OUTLOOK

These studies are meant as a first look at how coherent magnetic fields in the nearby ISM can cause anisotropic signals of cosmic rays. In particular, we have shown that such signals exist even with general coherent magnetic field configurations - they do not have to contain

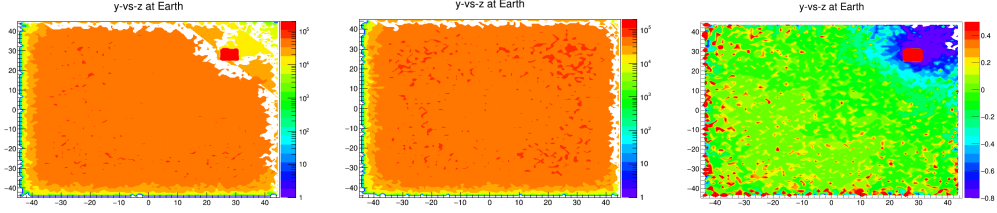


FIG. 5.— Skymaps, in terms of angle from the CR source. On the left is a skymap for model A of table 2. The plots were made with 2×10^6 sampled 10 TeV protons. The angular scale for such a large magnetic field region is roughly $5^\circ \times 5^\circ$ in extent. In the center is a skymap which was run with only diffusive propagation and no coherent regions. Fluctuations in this map are dominated by the finite statistics of the two million particles run in the simulation and would decrease as the number of particles is increased. On the right is a relative intensity map between the two other figures, which shows that the coherent field is easily distinguished above background fluctuations (the region actually has a relative intensity of roughly 25).

a cosmic-ray source. Coherent magnetic fields can increase the flux of particles in their direction in the sky by greater than three orders of magnitude, and even coherent fields far from a cosmic-ray source can contain several percent of the source’s emitted particles. These effects get stronger for smaller regions of coherent field and for regions with more turbulent diffusion. The less of the energy budget that is in coherent fields, the more important they are to propagation.

Other studies of the cosmic-ray anisotropies have seen similar results to those in section 5. In both Ahlers (2014) and Ahlers and Mertsch (2015), it was shown that turbulent structures in the local magnetic field can produce small-scale anisotropies through anisotropic diffusion. Giacinti and Sigl (2012) also showed that these local magnetic field structures could create such anisotropies. Similar work to our code was calculated in López-Barquero et al. (2015). However, that study primarily looked at particles with PeV-scale energies, where the Larmor radius and mean-free-path are on parsec scales, similar in size to the coherence length of the magnetic turbulence. An integral part of our code presented in this work was to consider lower-energy TeV-scale particles which have Larmor radii and mean-free-paths which are much smaller than coherence length of the structured magnetic fields. Full MC integration of these TeV particles is intractably slow, so this was why a hybrid diffusion+MC method was needed. Additionally, López-Barquero et al. (2015) assumed that the source population was diffuse, which allowed them to time-reverse incoming particles to get maps of the anisotropic sky. However, our code allows for general source distributions in which particular CR sources are dominating the anisotropy.

Due to the inclusion of anisotropic cosmic rays sources, our code cannot conveniently be time-reversed to create artificial “back-tracked” skymaps as was done in Lopez-Barquero et al 2015. Instead, we used the method suggested in that paper of increasing the size of the target to record those particles that pass “nearby”. Using this method, we can convert from our earth-proxy maps (in pc) to angular maps of the Earth sky. However, because of low statistics, we can only get a reasonable sample out to within 45 degrees of the source location.

We have made such maps, both in the case of our model A and in the case of no coherent magnetic fields. The relative intensity of the magnetic field geometry over a geometry without coherent fields at each angle is shown

in figure 5. As can be seen in that figure, the strength of the anisotropy in our geometry A is large, much larger than is currently observed at Earth. However, it is expected that this intensity can be affected by the details of the magnetic field strength and geometry and the source spectra and geometry. However, this early result indicates that similar relative intensity features to the observed anisotropy should be possible.

Further studies of the cosmic-ray anisotropies with anisotropic transport through coherent magnetic fields may yield more information about how these anisotropies behave. In addition to isolated regions of cosmic-ray excess, some excess regions are also seen as long, thin regions extending in declination. Also, the location of the cosmic-ray anisotropy seems to vary with cosmic-ray energy (Aartsen et al. (2013)). A more detailed study of these features may suggest details about the structure of the magnetic fields which are causing them. It is also possible that the interplay between coherent magnetic fields and turbulent magnetic fields may be related to these additional features of the anisotropy (Harding and Fryer (2015)).

The interaction between coherent and turbulent magnetic fields could also be important due to cross-fieldline transport for structures with narrow geometrical structures. In this case, the “beaming” effects we observed here may be somewhat smeared out and less significant. In future work with this code, we plan on addressing such issues, including having both coherent and turbulent fields in the same spatial regions. With the inclusion of such features, the code will be more broadly applicable and the effects of coherent field structures on the anisotropy will be better understood.

It is possible that some of the features of the observed anisotropy are coincident with the heliotail (Drury and Aharonian (2008); Lazarian and Desiati (2010)), which is a known region of nearby high magnetic field. Also, IBEX has recently begun surveying the magnetic field structure of the nearby galaxy. These structures, along with the observed cosmic-ray anisotropies, may be able to explain the local cosmic-ray flux and begin to study the sources which create these observed cosmic rays. We will consider this is a forthcoming publication (Harding and Fryer (2015)). Depending on the details of the local ISM, non-diffusive propagation can explain the observed TeV cosmic-ray anisotropy.

We thank Brenda Dingus and Fan Guo for useful dis-

cussions. Work at LANL was done under the auspices of the National Nuclear Security Administration of the U.S. Department of Energy at Los Alamos National Labora-

tory under Contract No. DE-AC52-06NA25396 through an IGPPS grant.

REFERENCES

- A. W. Strong and I. V. Moskalenko, *Astrophys. J.* **509**, 212 (1998), astro-ph/9807150.
- G. Giacinti and G. Sigl, *Phys.Rev.Lett.* **109**, 071101 (2012), 1111.2536.
- B. M. Gaensler, M. Haverkorn, B. Burkhart, K. J. Newton-McGee, R. D. Ekers, A. Lazarian, N. M. McClure-Griffiths, T. Robishaw, J. M. Dickey, and A. J. Green, *Nature* **478**, 214 (2011), 1110.2896.
- P. Barge, J. Millet, and R. Pellat, *Astrophys. J.* **284**, 817 (1984).
- P. Desiati and E. G. Zweibel, *Astrophys. J.* **791**, 51 (2014), 1402.1475.
- J. Giacalone and J. R. Jokipii, *Astrophys. J.* **520**, 204 (1999).
- R. C. Tautz, A. Dosch, F. Effenberger, H. Fichtner, and A. Kopp (2013), 1309.7836.
- R. C. Tautz, A. Shalchi, and A. Dosch, *Astrophys. J.* **794**, 138 (2014), 1408.6947.
- M. Hussein, R. C. Tautz, and A. Shalchi, *Journal of Geophysical Research (Space Physics)* **120**, 4095 (2015), 1505.05099.
- A. Shalchi, *Advances in Space Research* **56**, 1264 (2015), 1506.07169.
- P. C. Frisch and N. A. Schwadron, in *Outstanding Problems in Heliophysics: From Coronal Heating to the Edge of the Heliosphere*, edited by Q. Hu and G. P. Zank (2014), vol. 484 of *Astronomical Society of the Pacific Conference Series*, p. 42, 1310.2922.
- P. C. Frisch, A. Berdyugin, H. O. Funsten, A. M. Magalhaes, D. J. McComas, V. Piirola, N. A. Schwadron, D. B. Seriacopi, and S. J. Wiktorowicz, *Journal of Physics Conference Series* **577**, 012010 (2015a), 1409.5428.
- P. C. Frisch, A. Berdyugin, V. Piirola, A. M. Magalhaes, D. B. Seriacopi, S. J. Wiktorowicz, B.-G. Andersson, H. O. Funsten, D. J. McComas, N. A. Schwadron, et al., *Astrophys. J.* **814**, 112 (2015b), 1510.04679.
- N. A. Schwadron et al., *Science* **343**, 988 (2014).
- A. U. Abeysekara et al. (HAWC), *Astrophys. J.* **796**, 108 (2014), 1408.4805.
- M. Amenomori et al. (Tibet AS Gamma), *Astrophys.J.* **626**, L29 (2005), astro-ph/0505114.
- M. Amenomori (Tibet AS-gamma), *Science* **314**, 439 (2006), astro-ph/0610671.
- G. Guillian et al. (Super-Kamiokande), *Phys. Rev.* **D75**, 062003 (2007), astro-ph/0508468.
- A. A. Abdo et al., *Astrophys. J.* **698**, 2121 (2009), 0806.2293.
- M. Aglietta, V. V. Alekseenko, B. Alessandro, P. Antonioli, F. Arneodo, L. Bergamasco, M. Bertaina, R. Bonino, A. Castellina, A. Chiavassa, et al., *Astrophys. J. Lett.* **692**, L130 (2009), 0901.2740.
- J. Zhang, S. Zhang, and S. Cui (ARGO-YBJ), in *Proceedings, 31st International Cosmic Ray Conference (ICRC 2009)* (2009), p. 42.
- M. Amenomori, X. J. Bi, D. Chen, S. W. Cui, Danzengluobu, L. K. Ding, X. H. Ding, C. Fan, C. F. Feng, Z. Feng, et al., *Astrophys. J.* **711**, 119 (2010), 1001.2646.
- K. Munakata, Y. Mizoguchi, C. Kato, S. Yasue, S. Mori, M. Takita, and J. Kóta, *Astrophys. J.* **712**, 1100 (2010), 0911.1165.
- R. Abbasi, Y. Abdou, T. Abu-Zayyad, J. Adams, J. A. Aguilar, M. Ahlers, K. Andeen, J. Auffenberg, X. Bai, M. Baker, et al., *Astrophys. J. Lett.* **718**, L194 (2010), 1005.2960.
- J. K. de Jong (MINOS), in *Proceedings, 32nd International Cosmic Ray Conference (ICRC 2011)* (2012), vol. 4, p. 46, 1201.2621.
- S. Cui, *International Cosmic Ray Conference* **1**, 6 (2011).
- M. G. Aartsen, R. Abbasi, Y. Abdou, M. Ackermann, J. Adams, J. A. Aguilar, M. Ahlers, D. Altmann, K. Andeen, J. Auffenberg, et al., *Astrophys. J.* **765**, 55 (2013), 1210.5278.
- B. Bartoli, P. Bernardini, X. J. Bi, Z. Cao, S. Catalanotti, S. Z. Chen, T. L. Chen, S. W. Cui, B. Z. Dai, A. D'Amone, et al., *Astrophys. J.* **809**, 90 (2015).
- M. Amenomori et al. (Tibet AS Gamma), *Proc. 30th ICRC* pp. 1493–1494 (2007).
- A. Abdo et al., *Phys.Rev.Lett.* **101**, 221101 (2008), 0801.3827.
- R. Abbasi, Y. Abdou, T. Abu-Zayyad, J. Adams, J. A. Aguilar, M. Ahlers, D. Altmann, K. Andeen, J. Auffenberg, X. Bai, et al., *Astrophys. J.* **740**, 16 (2011), 1105.2326.
- M. Aartsen et al. (IceCube), *Astrophys.J.* **765**, 55 (2013), 1210.5278.
- G. Di Sciascio (ARGO-YBJ), *EPJ Web Conf.* **52**, 04004 (2013), 1303.2049.
- B. Bartoli et al. (ARGO-YBJ), *Phys. Rev.* **D88**, 082001 (2013), 1309.6182.
- L. Drury and F. Aharonian, *Astropart.Phys.* **29**, 420 (2008), 0802.4403.
- M. Malkov, P. Diamond, L. Drury, and R. Sagdeev, *Astrophys.J.* **721**, 750 (2010), 1005.1312.
- A. Lazarian and P. Desiati, *Astrophys.J.* **722**, 188 (2010), 1008.1981.
- K. Kotera, M. A. Perez-Garcia, and J. Silk, *Phys. Lett.* **B725**, 196 (2013), 1303.1186.
- J. P. Harding (2013), 1307.6537.
- O. Adriani et al. (PAMELA), *Phys.Rev.Lett.* **106**, 201101 (2011), 1103.2880.
- M. Ackermann et al. (Fermi LAT), *Phys.Rev.Lett.* **108**, 011103 (2012), 1109.0521.
- M. Aguilar et al. (AMS), *Phys.Rev.Lett.* **110**, 141102 (2013).
- T. Linden and S. Profumo, *Astrophys.J.* **772**, 18 (2013), 1304.1791.
- I. Cholis and D. Hooper, *Phys.Rev.* **D88**, 023013 (2013), 1304.1840.
- P. C. Frisch, *Space Sci. Rev.* **72**, 499 (1995).
- M. D. Kistler, H. Yuksel, and A. Friedland (2012), 1210.8180.
- V. Petrosian and S.-M. Liu, *Astrophys. J.* **610**, 550 (2004), astro-ph/0401585.
- C. L. Fryer, S. Liu, G. Rockefeller, A. Hungerford, and G. Belanger, *Astrophys. J.* **659**, 389 (2007), astro-ph/0609483.
- K. Mannheim and R. Schlickeiser, *Astron. Astrophys.* **286**, 983 (1994), astro-ph/9402042.
- C. D. Dermer, *Astrophys. J.* **295**, 28 (1985).
- J. P. Harding and C. Fryer (2015), *Work in Progress*.
- M. Ahlers, *Phys. Rev. Lett.* **112**, 021101 (2014), 1310.5712.
- M. Ahlers and P. Mertsch, *Astrophys. J.* **815**, L2 (2015), 1506.05488.
- V. López-Barquero, R. Farber, S. Xu, P. Desiati, and A. Lazarian (2015), 1509.00892.